

pubs.acs.org/cm Article

Resolving Chemical and Spatial Heterogeneities at Complex Electrochemical Interfaces in Li-Ion Batteries

Julia C. Hestenes, Richard May, Jerzy T. Sadowski, Naiara Munich, and Lauren E. Marbella*



Cite This: Chem. Mater. 2022, 34, 232-243



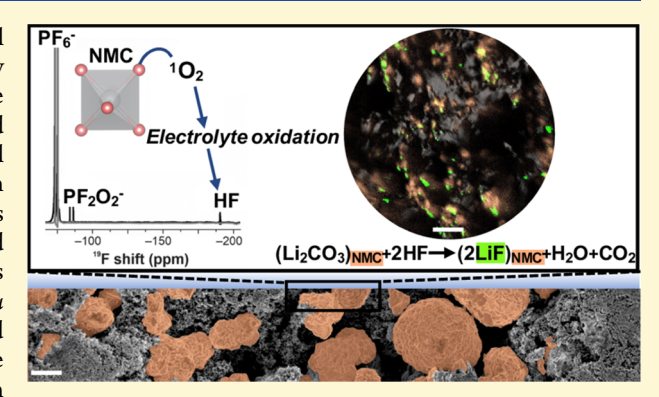
ACCESS I

Metrics & More

Article Recommendations

Supporting Information

ABSTRACT: The high specific capacities of Ni-rich transition-metal oxides have garnered immense interest for improving the energy density of Li-ion batteries (LIBs). Despite the potential of these materials, Ni-rich cathodes suffer from interfacial instabilities that lead to crystallographic rearrangement of the active material surface as well as the formation of a cathode electrolyte interphase (CEI) layer on the composite surface during electrochemical cycling. While changes in crystallographic structure can be detected with diffraction-based methods, probing the chemistry of the disordered, heterogeneous CEI layer is challenging. In this work, we use a combination of *ex situ* solid-state nuclear magnetic resonance (SSNMR) spectroscopy and X-ray photoemission electron microscopy (XPEEM) to provide chemical and spatial information, on the nanometer length scale, on



the CEI deposited on LiNi_{0.8}Mn_{0.1}Co_{0.1}O₂ (NMC811) composite cathode films. XPEEM elemental maps offer insight into the lateral arrangement of the electrolyte decomposition products that comprise the CEI and paramagnetic interactions (assessed with electron paramagnetic resonance (EPR) and relaxation measurements) in ¹³C SSNMR provide information on the radial arrangement of the CEI from the NMC811 particles outward. Using this approach, we find that LiF, Li₂CO₃, and carboxy-containing structures are directly appended to NMC811 active particles, whereas soluble species detected during *in situ* ¹H and ¹⁹F solution NMR experiments (e.g., alkyl carbonates, HF, and vinyl compounds) are randomly deposited on the composite surface. We show that the combined approach of *ex situ* SSNMR and XPEEM, in conjunction with *in situ* solution NMR, allows spatially resolved, molecular-level characterization of paramagnetic surfaces and new insights into electrolyte oxidation mechanisms in porous electrode films.

■ INTRODUCTION

Ni-rich cathode materials offer high energy densities (>200 mAh/g)^{1,2} while simultaneously reducing the amount of costly Co³ used in Li-ion batteries (LIBs). Despite these advantages, Ni-rich cathodes, such as LiNi_{0.8}Mn_{0.1}Co_{0.1}O₂ (abbreviated NMC811), suffer from severe thermal and interfacial^{2,4,5} instabilities during usage that prevent broad application. Degradation pathways in NMC811 cathodes include particle cracking, ⁵⁻⁸ gas evolution, ⁹⁻¹¹ surface reconstruction, ¹²⁻¹⁴ transition-metal dissolution, ^{5,15-17} and parasitic interfacial reactions with the electrolyte ^{4,18,19}—many of which are strongly coupled to one another. Changes in the crystallographic and secondary particle structure of Ni-rich NMCs are readily identified using diffraction- and imaging-based techniques. 12,13,20-24 For example, X-ray tomography and electron microscopy can detect crack formation in NMC secondary particles during electrochemical cycling. 6,25 Electrolyte molecules can then infiltrate these cracks and participate in side reactions that lead to poor capacity retention.⁵ Electron and X-ray diffraction measurements indicate that repeated cycling of NMC811 leads to oxygen depletion at the particle surface, forming a NiO reconstruction layer that blocks Li+

transport¹² and increases the charge-transfer resistance.²⁶ The associated oxygen evolution can be directly quantified using differential/on-line electrochemical mass spectrometry (DEMS/OEMS).^{27–29} Strongly oxidizing species generated during battery operation, such as molecular oxygen and freshly exposed Ni⁴⁺/Ni–O sites,^{4,30–33} can then go on to attack the electrolyte, leading to further performance degradation. The resulting electrolyte decomposition products deposit on the cathode surface, leading to a disordered, multiphase cathode electrolyte interphase (CEI)³⁴ layer that alters Li transport to the active material.

Unfortunately, characterizing the composition and the arrangement of the CEI layer, and correlating these features with battery performance, is exceptionally challenging due to

Received: September 15, 2021 Revised: December 10, 2021 Published: December 28, 2021





the complexity of composite cathode films. The cathodes used in technologically relevant LIBs contain active particles (e.g., NMC811) embedded in a heterogeneous matrix of conductive carbon and poly(vinylidene fluoride) (PVDF) binder, presenting issues with both chemical and spatial resolution in CEI characterization. 35-37 High chemical resolution is essential to distinguishing signals that arise from electrolyte decomposition products vs carbon additives in the composite. Both the CEI layer and the carbon additives are highly disordered and contain light elements (H, C, F) that are difficult to resolve with traditional surface science methods. Li salts and solvents from the electrolyte can get trapped in the porous cathode composite, leading to signal overlap with potential electrolyte decomposition products. In addition, spatial resolution in CEI characterization (e.g., measuring the location of electrolyte decomposition products as they deposit on the heterogeneous cathode composite) is important for determining the reactivity associated with the active particle vs the carbon additives. For example, a recent study suggested that surface Ni-O sites attack cyclic ethylene carbonate (EC) solvent, appending dehydrogenated EC molecules to the NMC811 surface. 18,33 Direct attachment of electrolyte decomposition products to the active particle is consistent with work from Gasteiger and co-workers that shows highsurface-area carbons do not evolve CO2 (from EC ring opening) in the absence of NMC particles.³⁶ While these reports strongly suggest that electrolyte oxidation occurs at the active particle surface, no direct evidence for CEI attachment at the active material was obtained. In contrast, several reports have identified electrolyte decomposition products on the carbon additives, 35,38,39 but it is not clear if these species decompose directly on the carbon/binder or if they are deposited on the composite in some other manner (e.g., during anode/cathode crosstalk, 40-43 in which Li+-solvating electrolyte decomposition products generated at the anode can migrate to the cathode and deposit in the CEI during cathode

Nuclear magnetic resonance (NMR) spectroscopy is a powerful, nondestructive tool to characterize electrochemical interfaces in their native operating environment. The high chemical resolution, especially for light elements (e.g., ¹³C), can be leveraged to determine the precise molecular structure of electrolyte decomposition products present in interphase layers. While solid-state NMR (SSNMR) has been used to characterize the composition of the electrode/electrolyte interphase (EEI) on the anode side of the battery, 44-49 substantially less work has focused on using SSNMR to characterize the CEI on the cathode. 41,50-52 Most industrially relevant cathode materials contain paramagnetic transition metals (e.g., Co, Mn, Ni, Fe). 53,54 Unpaired electrons from these paramagnetic substrates can couple to nuclei in the CEI layer, leading to fast nuclear spin relaxation and severe line broadening during NMR characterization, 53,55,56 which presents a technical challenge for detecting discrete compounds in the CEI with NMR. Traditional signal enhancement strategies used in SSNMR, such as ${}^{1}H \rightarrow {}^{13}C$ cross-polarization magic-angle spinning (CPMAS), do not work on paramagnetic cathodes due to fast relaxation during the CP step of the NMR experiment,⁵⁷ further hindering CEI characterization efforts.

Here, we show that by manipulating the Ni oxidation state in NMC811 cathode composites, we can determine the composition and arrangement of the CEI using SSNMR. We report that direct polarization of ¹³C nuclei in SSNMR

facilitates detection and compositional assignment of the CEI formed on NMC811 upon delithiation (charging of the battery). Electron paramagnetic resonance (EPR) spectroscopy indicates that during battery charging, oxidation of Ni^{2+/3+} to Ni⁴⁺ dilutes the paramagnetic matrix present in NMC811, greatly decreasing the magnetic susceptibility and enabling well-resolved SSNMR of organic species in the CEI. In particular, we show that carbonates directly bound to NMC particles (within approximately 1 nm of the NMC surface) can be discerned from CEI species spatially distant from NMC with SSNMR because NMC-bound carbonates produce a characteristic spinning sideband pattern in the NMR spectrum. These data indicate that SSNMR provides radial information (as measured from the surface of the NMC particle) on CEI arrangement, where compounds closest to the NMC811 active particles exhibit spinning sidebands. SSNMR measurements are complemented with X-ray photoemission electron microscopy (XPEEM) elemental imaging experiments, which reveal the lateral arrangement of LiF and the organic decomposition products in the CEI of the composite cathode film. While LiF, carboxy-containing Li salts, and Li₂CO₃ selectively deposit on NMC811 particles, alkyl carbonates are randomly distributed on the composite (i.e., indiscriminately on the active material and the carbon additives), possibly due to their more soluble nature and/or anode/cathode crosstalk. Soluble electrolyte oxidation products (e.g., short-chain alkyl carbonates, vinyl species, and HF) from side reactions at the NMC surface are identified with ex situ and in situ solution NMR spectroscopy, allowing us to rationalize the distribution of organic small molecules in the CEI.

MATERIALS AND METHODS

Materials. Li metal ribbon (0.75 mm thick), 1 M LiPF₆ in ethylene carbonate/dimethyl carbonate (EC/DMC 1:1 v/v, LP30, battery grade), 1-methyl-2-pyrrolidinone (NMP, anhydrous, 99.5%), KBr (\geq 99.0%), silica gel (ultrapure, 60–200 μ m), and Au powder (≥99.9%, particle size \leq 10 μ m) were purchased from Sigma-Aldrich. DMSO- d_6 (\geq 99.9%) was purchased from Cambridge Isotope Laboratories. Prior to use, DMSO- d_6 was dried over molecular sieves in an Ar-filled glovebox ($O_2 < 0.1$ ppm, $H_2O < 0.5$ ppm) for 48 h. Both KBr and silica gel were dried at 60 °C for 7 days before bringing into the glovebox for the preparation of SSNMR samples. The surface oxide layer on Li metal was scraped off prior to assembly in Li/NMC half-cells. All other chemicals were used as received. NMC811, NMC532, and NMC111 cathode powders were purchased from MTI Corporation. All cathode powders were stored in an Ar-filled glovebox. Carbon super P C45 and PVDF were purchased from MTI Corporation and used as received.

Electrode Fabrication. Cathode films for each NMC composition were prepared by first hand grinding a 10:1 ratio (by mass) of NMC:carbon super P. This mixture was added to a solution of PVDF binder in NMP at a 10:1 ratio (by mass) of NMC + C:PVDF to create a viscous slurry. The slurry was cast onto an Al current collector (25 μm thick, MTI Corporation) using a 150 μm doctor blade and dried at 100 °C under vacuum overnight. The dried film was punched into 12.7 mm diameter disks to use in cell assembly. Once dried, cathode films were stored in an Ar-filled glovebox to minimize exposure to air and moisture. Typical mass loadings of active material (e.g., NMC811) per cathode were 8–13 mg/cm². These electrodes were used for all electrochemical testing and then extracted for EPR, NMR, or XPEEM characterization.

Electrochemistry. Electrochemical tests were conducted using 2032 coin cells assembled in an Ar-filled glovebox with a 12.7 mm Li metal disc as the anode and NMC composite films (see Electrode Fabrication) as the cathode. Each cell used a Whatman glass microfiber (GF/A) separator and was cycled in \sim 0.2 mL of battery

grade, LP30 electrolyte. Galvanostatic cycling experiments were performed at C-rates of C/10 or C/5 (based on theoretical capacities of 275, 278, and 279 mAh/g for NMC811, NMC532, and NMC111, respectively) between 3.0 V and various upper cutoff voltages (the maximum upper cutoff voltage used for NMC811 was 4.6 V vs Li⁺/Li).

Solid-State NMR Spectroscopy. SSNMR experiments were performed at room temperature on a Bruker Avance NEO 600 MHz spectrometer equipped with a 1.6 mm HFXY MAS Phoenix NMR probehead. To prepare samples for SSNMR, Li/NMC half-cells were disassembled in the glovebox at the desired state of charge (e.g., at the end of charge at 4.6 V). After cell disassembly, the cathode film was scraped from the Al current collector and dried under vacuum overnight to remove residual solvent. Electrodes were not washed during sample preparation to preserve the highly sensitive interphase layer. Each sample was mixed with KBr powder or silica gel in a roughly 1:1 ratio by mass in a mortar and pestle until homogenized to fill a 1.6 mm o.d. ZrO2 rotor. All experiments were performed at a 28 kHz MAS frequency, unless otherwise noted. ¹H and ¹³C spin echo spectra were collected using a rotor-synchronized spin echo pulse sequence $(90^{\circ} - \tau - 180^{\circ} - \tau - \text{acquire}, \text{ with } \tau \text{ set to } 1 \text{ rotor period})$ with a recycle delay of 10 and 0.8 s, respectively. While direct polarization of ¹³C SSNMR of diamagnetic samples often requires long acquisition times, fast T_1 relaxation of the CEI on the paramagnetic cathode let us to acquire ¹³C SSNMR more quickly using a short recycle delay of 0.8 s (recycle days were varied from 0.8 to 10 s to determine the optimal value). For ¹³C SSNMR, ¹H decoupling was performed with TPPM at \sim 100 kHz. ¹H T_1 measurements of the CEI on NMC811 (Table S1), show that relaxation of ¹H nuclei present on NMC811 composites is too short (on the order of ms) to perform CPMAS experiments (the contact pulse is typically applied for ms). ¹³C SSNMR spectra presented in this study were acquired over a period of about 14-18 h per sample, equivalent to ~100 000 scans per sample. Single-pulse ⁷Li SSNMR spectra were collected using a single 90° pulse-acquire sequence with a pulse length of 2.6 μ s, 5 s recycle delay, and 128 scans. All SSNMR spectra presented are normalized to the maximum peak height in a given spectrum, unless otherwise noted. ¹H NMR was externally referenced to adamantane at 1.85 ppm. ¹³C NMR was externally referenced to the high frequency peak of adamantane at 38.5 ppm. ⁷Li NMR was externally referenced to LiF at −1 ppm or Li₂CO₃ at 0 ppm. We attempted to collect ¹⁹F SSNMR from cycled composite films, but no signals from common electrolyte decomposition products (e.g., LiF at -204 ppm) could be assigned, likely due to the higher gyromagnetic ratio of 19 F compared to 13 C (γ_{19F} = $2.52 \times 10^8 \text{ rad/sT}$ compared to $\gamma_{13C} = 6.73 \times 10^7 \text{ rad/sT}$) and the close proximity of LiF to the NMC811 surface. As these samples were unwashed, only 19F SSNMR signals from the PVDF binder and residual PF₆⁻ salt were detected, which is expected because these species are highly concentrated in the sample and are further away from the NMC substrate compared to CEI products.

EPR Spectroscopy. X-band EPR measurements were performed on an ESR-5000 spectrometer manufactured by Freiberg Instruments for Bruker, sold by Rotunda Scientific Technologies. The spectrometer has a microwave frequency of 9.47 GHz at room temperature. All measurements employed a B-field sweep from 50 to 650 mT, microwave power of 0.3162 W, 0.5 mT modulation amplitude with 100 kHz frequency, and a 60 s sweep time with 1 scan. As-received NMC811 powder was packed into a Bruker 1.9 mm rotor. Dried cathode samples extracted from Li/NMC half-cells were ground with KBr and packed into either a Bruker 1.9 mm or Varian 1.6 mm ZrO₂ rotor. The rotor was placed into a quartz EPR tube for measurement. Because the content of carbon was kept constant in the cathodes and is not electrochemically active (10 wt % of the composite film), spectra are normalized to the peak from conductive carbon.

XPEEM. Prior to electrochemical cycling, NMC811 cathodes were prepared by pressing composite cathode films at 2 tons in a hydraulic press (Specac), resulting in a pressure of 40 MPa, to flatten the sample for XPEEM. After cycling, cathode films were removed from the batteries in the glovebox and dipped into 1 mL DMC twice for 3 s

each to remove residual salts and minimize surface layer outgassing in the vacuum chamber. Cathode films were then dried under vacuum overnight to remove residual solvent. Samples were double-sealed in airtight pouches under Ar and transferred to the XPEEM facility at Brookhaven National Laboratory (BNL) for measurement. Samples were mounted on XPEEM holders in an Ar-filled glovebox and transferred to the XPEEM vacuum chamber using an air-free suitcase.

Pixel-wise X-ray absorption spectra (XAS) were obtained by recording a series of XPEEM images at each energy in a given absorption edge range at sequential increments of 0.2 eV. Ni L-edge spectra were referenced to the low-energy L₃ edge peak, which has a reported value of 853.5 eV.⁵⁸ Other edges were translated accordingly, except the C K-edge which referenced the lowest-energy peak, assigned to conductive carbon, at 285.4 eV. 37,59 Local XAS spectra can be extracted by plotting the intensity of a given spatial region (set of pixels) at each energy. For example, for Ni L-edge, 152 XPEEM images were acquired from 850 to 880 eV. XPEEM elemental contrast images were obtained by subtracting the pre-edge image from the desired X-ray absorption energy. The C K-edge image at 292.8 eV was extracted to display the spatial distribution of conductive carbon. The pre-edge image at 280.0 eV was then subtracted, yielding the final elemental map of conductive carbon. The same procedure was conducted for other elements presented in these elemental maps: Ni L-edge at 853.5 eV for $Ni^{2+/3+}$ and 855.9 eV for Ni^{4+} (850.0 eV preedge subtracted), and F K-edge at 691.7 eV for PVDF (685.0 eV pre-

Acquisition of C K-edge spectra in XPEEM is challenging due to strong absorption at this edge from carbon impurities in the X-ray optics as well as the Au mesh typically used to normalize the spectra of absorption edges of other elements. To make use of these spectra, we adopted the approach reported by El Kazzi and co-workers where Au microparticles are deposited on a small portion of the surface of a pristine NMC811 film for internal referencing prior to pressing the sample. The local C K-edge spectrum at the Au particle was extracted and used to normalize all other local C K-edge spectra from the cathode films to yield the true C K-edge spectrum. Each spectrum presented was normalized to a maximum intensity of one unless otherwise noted.

Ex and In Situ Solution NMR. For ex situ solution NMR measurements, Li/NMC811 half-coin cells were disassembled in the glovebox after cycling. The glass fiber separator was soaked in 1 mL DMSO- d_6 for 5 min and compressed using clean tweezers to fully extract electrolyte from the separator. The resulting solution was pipetted into a 5 mm airtight J-Young NMR tube for analysis. All solution NMR experiments were performed on a Bruker Avance III 400 spectrometer equipped with a triple resonance broadband observe (TBO) probehead. One-dimensional (1D) 1 H (30° single pulse, 1 s recycle delay, 16 scans, internally referenced to residual DMSO at 2.5 ppm) and 19 F (30° single pulse, 2 s recycle delay, 32 scans, internally referenced to PF $_6$ at -74.5 ppm) were recorded at room temperature. Three replicate samples were measured.

For in situ solution NMR measurements, we designed a Li/ NMC811 tube cell to collect ¹H and ¹⁹F NMR during electrochemical cycling. The Li/NMC811 cell was galvanostatically cycled for 10 cycles and placed in the NMR magnet for measurement. This method eliminates the need to disassemble the working cell for NMR and expose electrolyte decomposition products to DMSO-d₆ NMR solvent for locking. The in situ cell was assembled as a flooded cell in a chemically resistant FEP NMR tube liner with o.d. = 3.65 mm and i.d. = 3.15 mm that was purchased from Wilmad Glassware. An NMC811/C45/PVDF/NMP cathode slurry was cast on an Al substrate and dried overnight in vacuo. Once dried, a 2.5 mm wide × 22 cm long section was cut out of the film such that only the bottom ~2 cm was covered with the NMC811 composite. This method allows for the Al substrate to serve as both a current collector for the NMC and lead for electrochemical connection, similar to the approach reported by Nowak and co-workers. 60 Active material loading was estimated such that the first cycle was consistent with C/ 10 cycling (ca. 1–2 mg). For the anode, a 2 mm wide \times 2 cm long piece of Li was hammered onto Cu mesh. The Cu mesh was

connected to a 22 cm long pure Cu wire via a heat-shrink, chemically resistant electrical insulation tubing. The heat-shrink tubing prevented cell shorting along the length of the NMR tube. The Li metal was wrapped in a single layer of Celgard 2325 separator. Prior to electrode insertion, 300 $\mu\mathrm{L}$ of LP30 was pipetted into the tube liner. Electrodes were inserted into the tube such that the ends were 25 mm from the bottom of the FEP tube. It is important that the electrodes remain outside the receiver coil (coil length 23.85 mm) during NMR measurement to be able to obtain a high-quality shim for satisfactory resolution in ¹H NMR. The cell was cycled for 10 full cycles at C/10 between 3.0 and 4.6 V. After cycling, the tube cell was disconnected, submerged into a 5 mm glass NMR tube containing 0.1 mL of DMSO-d₆ and immediately brought to the spectrometer for measurement of the electrolyte contents. NMR acquisition parameters are the same as described above for ex situ solution NMR, except 64 scans were used for $^{19}\mathrm{F}$ acquisition. The high sensitivity of $^{1}\mathrm{H}$ and $^{19}\mathrm{F}$ NMR allowed us to collect spectra in less than 3 min. Lowconcentration ¹H species with chemical shifts between 2.5 and 5.5 ppm cannot be discerned with this method since this region is dominated by the electrolyte solvent signals (the bulk component of the sample, Figure S16).

Background/Theory. In paramagnetic systems, unpaired electrons can interact with nearby nuclei, leading to fast nuclear relaxation behavior. These interactions scale with the magnetic moment of the paramagnet, the electron-nuclear interspin distance (r^{-3}) , and gyromagnetic ratio (γ) of the observe nucleus.^{54,57} As a result, nuclear coupling with electronic spins is strongest when in close proximity to unpaired electrons and increases for high γ nuclei (e.g., 1 H, 19 F) compared to low γ nuclei (e.g., 13 C). In SSNMR, two nuclear relaxation processes influence the resulting SSNMR signal acquisition: spin-lattice (T_1) and spin-spin (T_2) relaxation times, both of which typically decrease when near unpaired electrons. The time it takes for the spin system to reach thermal equilibrium in the external field, B_0 , is typically defined as $5 \times T_1$. Therefore, T_1 is proportional to how long one must wait between individual NMR measurements during signal averaging. In paramagnetic systems, T_1 can be very rapid (on the timescale of ms), allowing fast interscan repetition (i.e., recycle delays) that leads to short NMR experiment times. T_2 relaxation is inversely proportional to the full width at half-maximum (fwhm) of the resulting NMR signal. T2 values are also very short in paramagnetic systems (on the order of μ s),⁶¹ leading to broad NMR lineshapes compared to diamagnetic compounds. In magicangle spinning (MAS) SSNMR experiments, these broad lineshapes are broken up into a spinning sideband pattern (often denoted with asterisks) that envelope the peak breadth observed under static conditions. Each spinning sideband is separated by the MAS frequency. The isotropic resonance is invariant of the spinning frequency and is used in NMR to assign chemical environments, akin to the isotropic resonance observed in solution NMR. Consequently, as the MAS frequency changes, the isotropic resonance remains constant, while the separation between individual sidebands changes.

Prior work from our group on Li₂RuO₃ model cathodes indicates that quenching paramagnetism in the active material facilitates SSNMR characterization of the CEI layer generated during electrochemical cycling of layered transition-metal oxide cathodes. 41 In this work, we hypothesize that oxidation of paramagnetic $\mathrm{Ni}^{2+/3+}$ to diamagnetic Ni4+ in NMC811 composite films will similarly reduce the magnetic susceptibility and the resulting electron-nuclear coupling between the substrate (NMC) and the CEI layer, allowing us to acquire high-resolution SSNMR of the CEI. To test this hypothesis, we can (i) directly monitor changes in paramagnetism of the composite and (ii) measure changes in nuclear spin relaxation in the CEI as a function Ni oxidation state. In the first instance, changes in the magnetic properties of NMC811 during lithiation/delithiation are measured with EPR spectroscopy, which is sensitive to the presence of paramagnetic centers and their exchange interactions. The area under the EPR curve represents the number of unpaired electrons in the sample, which is proportional to the magnetic susceptibility of the sample. In the second case, weakened paramagnetism of the composite cathode substrate upon delithiation

is expected to increase the T_1 and T_2 relaxation times of the appended CEI layer, where longer relaxation times are expected to mitigate paramagnetic line broadening and the associated poor chemical resolution in SSNMR. In contrast, lithiation (discharge) of NMC811 is expected to increase paramagnetic interactions between the substrate and the CEI, leading to signal dephasing in SSNMR. Accordingly, both EPR spectroscopy of the bulk NMC as well as T_1 measurements of the CEI as a function of the NMC811 charge state are presented in the following section.

RESULTS

To provide context for the SSNMR measurements of the CEI on NMC811, we start by investigating the magnetic properties of composite cathode films at different states-of-charge (SoC) and different numbers of cycles. Figure 1 shows the EPR

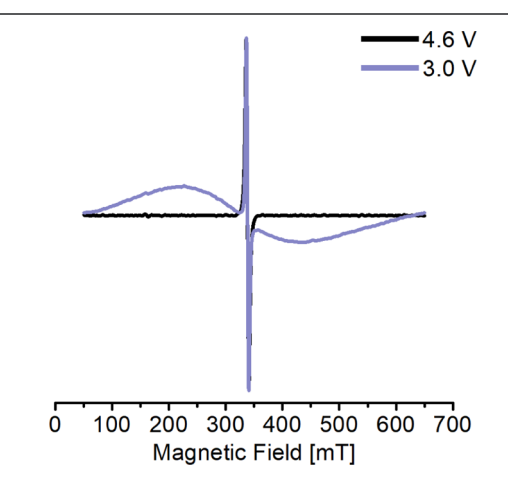


Figure 1. X-band EPR spectra of NMC811 composites after the first charge at C/10 to 4.6 V vs Li/Li^+ (black line) and the corresponding discharge to 3.0 V vs Li/Li^+ (purple line). The sharp peaks in the center of the spectra correspond to conductive carbon in the composite, whereas the broad lineshape observed upon discharge is assigned to NMC811.

spectra of NMC811/C/PVDF (80:10:10) composites obtained after discharging (3.0 V vs Li/Li⁺, purple) and charging (4.6 V vs Li/Li⁺, black) in Li half-cells. Both the charged and discharged samples yield a narrow resonance that is characteristic of unpaired electrons in the conductive carbon (Figure S1). 63,64 The discharged sample shows a broad resonance from the network of paramagnetic transition-metal cations in NMC811. We expect that the formal oxidation states in NMC811 are LiNi_{0.1}²⁺Ni_{0.7}³⁺Mn_{0.1}⁴⁺Co_{0.1}³⁺O₂, where the paramagnetic centers in the material include Ni³⁺ (S = 1/2), Ni²⁺ (S = 1), and Mn⁴⁺ (S = 3/2). Co³⁺ (S = 0) is diamagnetic and thus, EPR inactive. Therefore, we assign the broad signal observed at 3.0 V to Mn⁴⁺-Ni²⁺ exchange coupling interactions in the active material, $^{64,67-71}$ which is supported by control experiments comparing NMC811 with NMC532, NMC111, and LNMO (LiNi_{0.5}Mn_{1.5}O₄) (Figures S2 and S3).

Upon charging to 4.6 V in the first cycle, the EPR signal from NMC811 is quenched, while the signal from conductive carbon is still present (Figure 1). The persistence of the EPR signal from conductive carbon is expected because the carbon additives are not electrochemically active. Decreased EPR signal from the active material in the cathode composite is consistent with the oxidation of Ni^{2+}/Ni^{3+} (paramagnetic) to Ni^{4+} (S=0, diamagnetic) that occurs during delithiation. ^{22,68,69} Since the Mn⁴⁺ (S=3/2) and Co³⁺ (S=0) are

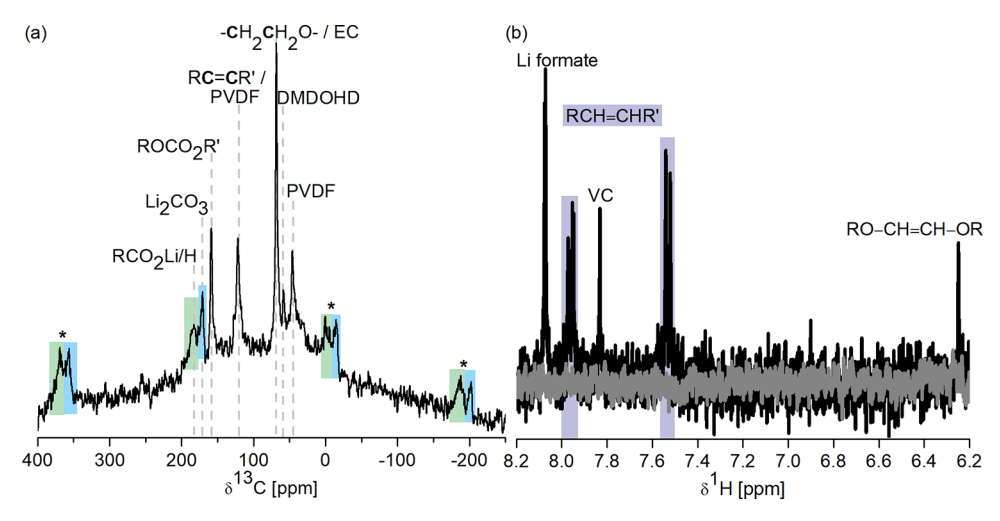


Figure 2. (a) Direct polarization ¹³C MAS SSNMR of an NMC811 cathode film that underwent 50 galvanostatic cycles at C/10 and was dissembled at 4.6 V vs Li/Li⁺. MAS frequency = 28 kHz. Asterisks denote spinning sidebands. (b) *In situ* solution ¹H NMR from an NMC811/Li battery in an NMR tube cell after 10 galvanostatic cycles at C/10 between 3.0 and 4.6 V (black) overlaid with an NMR spectrum of the pristine electrolyte (grey).

not redox-active, 31,72,73 the EPR signal from NMC811 disappears as the bulk oxidation state of the transition-metal centers are oxidized to form diamagnetic Ni⁴⁺. Paramagnetic Mn⁴⁺ cannot couple with diamagnetic Ni⁴⁺, decreasing the observable EPR signal.⁶⁴ The gradual decay in EPR signal upon charging NMC811 composites is shown in Figure S4, where the EPR signal of the NMC disappears at voltages \geq 4.2 V. This result supports that the net magnetic susceptibility of the bulk sample decreases with increasing SoC, as the content of Ni⁴⁺ in the transition-metal layer increases. The proportion of Ni⁴⁺ in the sample after the first charge to 4.6 V can be estimated from the specific charge capacity in the second cycle compared to the theoretical capacity of NMC811. (The specific capacity in the first charge is arbitrarily high from CEI formation/electrolyte oxidation, so the specific capacity from the second charge more accurately estimates how many Li ions were removed/reinserted in the first cycle, during which less side reactions are expected.) With the second charge of this cell yielding a specific capacity of 222 mAh/g, which is ~81% of the theoretical specific capacity (275 mAh/g), we estimate that the charged NMC sample in Figure 1 contains a stoichiometry $\text{Li}_{0.19}\text{Ni}_{0.19}^{2+/3+}\text{Ni}_{0.81}^{4+}\text{Mn}_{0.1}^{4+}\text{Co}_{0.1}^{3+}\text{O}_2$, indicating that most of the Ni is in the 4+ oxidation state and the network of paramagnetic centers is dilute.

A very low intensity, broad EPR signal, reminiscent of the active material at discharge, appears after 50 galvanostatic cycles in the charged state (Figure S5) that likely corresponds to surface reconstruction after repeated lithiation/delithiation. From the specific charge capacity of the 50th cycle (Figure S6, 159 mAh/g), we estimate that the stoichiometry of the NMC is $\text{Li}_{0.42}\text{Ni}_{0.42}^{2^{+}/3^{+}}\text{Ni}_{0.58}^{4^{+}}\text{Mn}_{0.1}^{4^{+}}\text{Co}_{0.1}^{3^{+}}\text{O}_{2}$, with an increased concentration of paramagnetic centers that manifest as a broad signal in EPR. Terminal Ni⁴⁺ sites on the surface of NMC811 are highly unstable, and are reduced to form a Ni²⁺-O rocksalt layer that has been widely reported in the literature 12,13,31,58,74-76 and can be visualized in XPEEM maps (see below, Figure 3). The Ni²⁺ on the active particle surface can undergo exchange coupling with neighboring Mn⁴⁺ sites, leading to the low-intensity, exchange-narrowed EPR spectrum. The NiO layer represents a small proportion of the overall sample and based on the EPR intensities, we conclude

that even after 50 cycles, the magnetic susceptibility of the substrate is substantially smaller than that observed upon discharge. Strong paramagnetism at discharge and weaker paramagnetism at charge is also supported by 1 H T_1 relaxation measurements of the corresponding CEI layer. For example, 1 H T_1 values for the CEI on NMC811 composites upon charging to 4.6 V are two orders of magnitude greater than that observed upon discharge (Table S1, Figure S7), and thus, charged Ni-rich cathode samples are expected to produce better-resolved NMR spectra for CEI detection. However, the T_1 of NMC at charge is still relatively fast (10^{-1} s) compared to diamagnetic materials due to weak paramagnetism associated with residual (but dilute) paramagnetic centers such as Mn^{4+} and $\mathrm{Ni}^{3+/2+}$ from incomplete delithiation and surface NiO.

With an understanding of the paramagnetic properties of NMC811 composites in hand, we next use ¹³C SSNMR to characterize the organic CEI that forms after 50 galvanostatic cycles when cells are disassembled at 4.6 V, where the paramagnetism is the lowest (Figure 2a). Representative voltage profiles collected during the 1st and 50th cycles of Li/NMC811 half-cells are shown in Figure S6. As expected from our EPR measurements, the weak paramagnetism associated with NMC811 at charge enables high-resolution ¹³C SSNMR, where a variety of electrolyte decomposition products are observed. The resonance at ~171 ppm is assigned to Li₂CO₃ and the broad resonance centered at ~185 ppm is characteristic of structures containing carboxy groups (RCO₂Li/H). 44,48 Carboxy-containing structures can be generated from electrolyte oxidation reactions at the cathode that also produce CO₂ and water. ¹⁹ In situ ¹H solution NMR shows the presence of Li formate at 8.08 ppm, which is likely generated from the reduction of CO₂ gas at the anode 19 side of the battery (Figure 2b). The large $^{13}\bar{\text{C}}$ resonance at \sim 69 ppm is assigned to poly(ethylene oxide) (PEO)-type moieties that are present in the CEI layer and/or residual ethylene carbonate (EC).⁴⁸ The ¹³C resonance at ~159 ppm is assigned to the carbonyl carbon (ROCO2R') in alkyl carbonates and/or residual EC/DMC. We also observe a small ¹³C resonance at ~58 ppm that corresponds to DMDOHD (dimethyl 2,5dioxahexanedioate), a soluble decomposition product of DMC

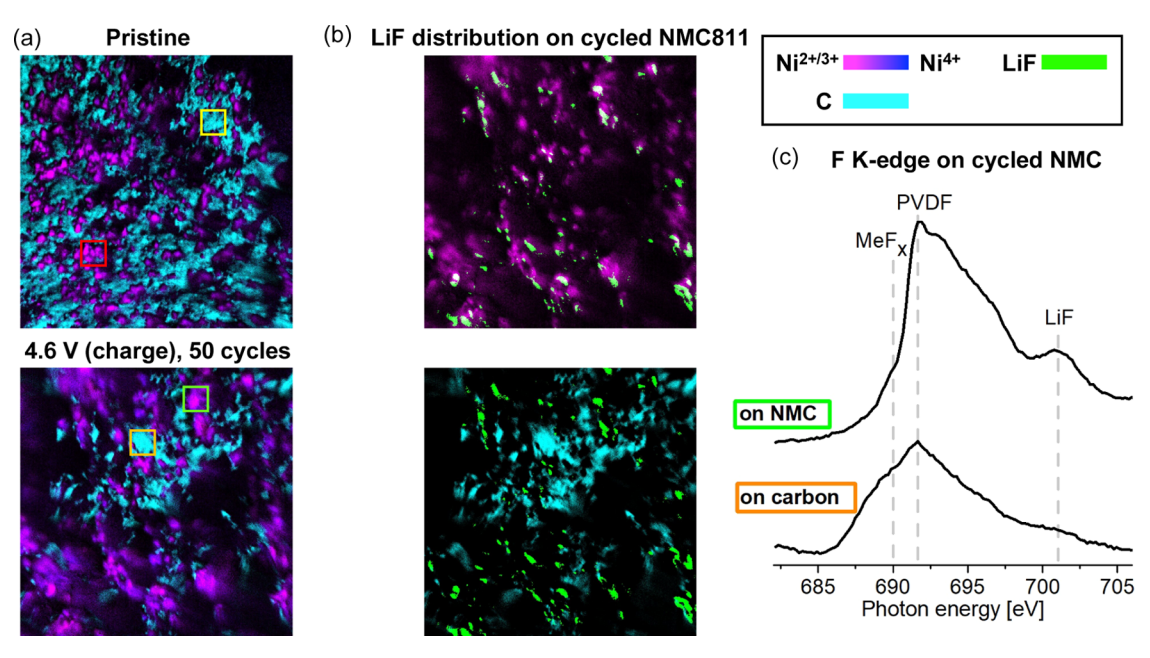


Figure 3. (a) Elemental XPEEM images (area = $30 \times 30 \ \mu m^2$) of pristine NMC811 (top) and NMC811 composites after 50 galvanostatic cycles (bottom) at C/5 and disassembled at 4.6 V vs Li/Li⁺. Ni elemental maps (dark blue/magenta color) show the distribution of NMC particles in the composite. Cyan indicates regions of conductive carbon. (b) Elemental XPEEM images from the cycled sample from (a) showing the LiF elemental map (green) extracted from the XPEEM image at 702 eV. The top image shows the Ni²⁺ map (magenta) overlaid with the LiF map (green). The bottom image shows the regions corresponding to conductive carbon (cyan) and LiF (green). The elemental maps in (b) indicate that LiF is selectively deposited on the surface of NMC811 particles. (c) F K-edge local XAS spectra extracted from the cycled composite shown in (a) with regions corresponding to NMC811 particles and conductive carbon highlighted with green and orange boxes. Local C K-edge spectra for these regions and the red/yellow boxes in the pristine sample in (a) are shown in Figure S13.

solvent. 60,77,78 The assignment of DMDOHD in 13C SSNMR is supported by the observation of DMDOHD in ex situ ¹H and ¹³C solution NMR (Figure S8). The small resonance at \sim 32 ppm is assigned to the aliphatic (RCH₂CH₂R') environment in short-chain decomposition products such as lithium butylene dicarbonate (LBDC) and/or Li succinate. 47,48 PVDF binder in the composite produces ¹³C resonances at 45 and 122 ppm, corresponding to the $-\underline{C}H_2CF_2$ and -CH₂CF₂- groups in PVDF, respectively. However, careful inspection of the relative ratios of $-\underline{C}H_2CF_2-/-CH_2\underline{C}F_2-$ in pristine PVDF (Figure S9) compared to our cathode film indicates that the resonance at 122 ppm is larger than expected. Based on this increased ¹³C signal intensity at 122 ppm, we believe that this resonance does not solely arise from PVDF, and is likely due to the presence of unsaturated/vinyl compounds (RC=CR') that also appear at this chemical shift^{46,79} and are observed during in situ ¹H solution NMR measurements (Figure 2b). The in situ ¹H solution NMR shows the presence of vinylene carbonate (1H shift at 7.83 ppm (s)) 19,45 and Li formate (1 H shift at 8.08 ppm (s)). 19 The singlet at 6.25 ppm is assigned to a symmetric RO-HC= CH-OR group 80,81 that likely appears at lower frequency than VC because it is a linear fragment. We also observe two unique asymmetric RHC=CHR' groups 45 (both 1H shifts appear as doublets with one shift centered at 7.53 ppm and the other at 7.96 ppm with J_{H-H} = 8.15 Hz; we suspect that the difference in chemical shift arises from different R substituents). These vinyl species are not detected with ex situ solution NMR, suggesting that they are highly reactive. The formation of unsaturated compounds in the electrolyte is thus consistent with the detection of a C=C resonance at approximately 122 ppm in ¹³C SSNMR (Figure 2a).

Analysis of the full spectral breadth of Figure 2a shows that only certain ¹³C resonances from the CEI on NMC811 composites exhibit spinning sidebands that span a wide spectral range (e.g., Li₂CO₃ (shaded blue) and carboxycontaining structures (shaded green) in Figure 2). Since paramagnetic coupling to NMR-observe nuclei is distancedependent $(r^{-3}$ relationship), we expect that compounds closest to the paramagnetic NMC particles will exhibit more line broadening (and thus a broad sideband pattern) than those deposited further away. 54,55,57,82 However, the exact location of these compounds in the composite is not immediately apparent because EPR (Figure 1) indicates that both NMC811 and conductive carbon contain unpaired electrons that could induce these sideband patterns. To determine if NMC811, conductive carbon, or both components contribute to the observed SSNMR sidebands in Figure 2a, we performed a series of control experiments where bulk Li₂CO₃ was attached (via mechanical milling) to NMC811 or conductive carbon (at a 1:2 ratio of Li₂CO₃:NMC811 or conductive carbon). The ⁷Li SSNMR spectrum of pristine Li₂CO₃ shows a relatively narrow sideband pattern, with an fwhm of 1030 Hz (Figure S10). After ball-milling with conductive carbon, the fwhm of the ⁷Li SSNMR resonance for Li₂CO₃ increases slightly to 1175 Hz, likely due to a minor increase in paramagnetic anisotropy from interaction with delocalized electrons on the conductive carbon. The largest change in line broadening is observed after ball-milling Li₂CO₃ with NMC811, where we see a 7Li fwhm of approximately 1580 Hz. Likewise, the corresponding ¹³C SSNMR spectrum of Li₂CO₃/NMC811 (Figure S11) shows a sideband pattern that spans from +300 to -200 ppm, similar to that observed in ¹³C SSNMR of the CEI on NMC811 (Figure 2a). No sidebands are observed for Li₂CO₃/carbon and we had to use a

longer recycle delay (10 vs 0.8 s) to detect 13 C SSNMR of $\text{Li}_2\text{CO}_3/\text{carbon}$, which is consistent with slower T_1 relaxation times for Li_2CO_3 attached to carbon rather than NMC811 (i.e., less paramagnetic relaxation enhancement). The similarities between the spinning sideband patterns and the nuclear relaxation rates for the $\text{Li}_2\text{CO}_3/\text{NMC811}$ control sample and the CEI on NMC composite films strongly suggest that the spinning sideband patterns observed for Li_2CO_3 and carboxy moieties in Figure 2a arise from the attachment to NMC811 particles, 55 and not conductive carbon.

To approximate the radial distance between the CEI compounds identified with SSNMR and the NMC substrate, we performed a back-of-the-envelope calculation, based on electron-nuclear coupling (see the Radial Distance Estimation section on page 15 in the Supporting Information). Our estimate shows that the distance between unpaired electrons at the surface of the NMC substrate (e.g., from the NiO rocksalt layer) and compounds in the CEI that generate the spinning sideband patterns shown in Figure 2a (RCO₂Li/H and Li₂CO₃) is approximately 1 nm. Therefore, we expect that RCO₂Li/H and Li₂CO₃ are both located within the first 1 nm of the CEI, nearest to NMC811. This distance-dependence falls off rapidly and CEI compounds that do not show a spinning sideband pattern are likely located outside of this inner, 1 nm CEI layer, either in the outer CEI or on the carbon additives.

The lack of a spinning sideband pattern for certain CEI components in ${}^{13}\text{C}$ SSNMR (vinyl compounds, PEO/residual solvent, DMDOHD) indicates that these compounds are further from the NMC811 surface. Yet, these species could be located (1) in the outer CEI layer that lies directly on NMC811 particles or (2) on the surface of the carbon additives in the composite where they do not interact with unpaired electrons from the paramagnetic NMC particles. To understand the lateral distribution of the CEI on NMC811 films, we used XPEEM elemental imaging (Figure 3). In XPEEM, XAS spectra are recorded as a function of position on the composite surface, allowing us to map the location of active particles (through Ni L-edge spectroscopy), conductive carbon (C K-edge spectroscopy), PVDF binder (F K-edge spectroscopy), and CEI components (from unique binding energies in C and F K-edge spectroscopies). Figure 3 shows elemental XPEEM images depicting the lateral arrangement of NMC811 particles (magenta/dark blue, depending on Ni oxidation state) with respect to conductive carbon (cyan). Ni L-edge XAS spectra (Figure S12) were used to locate active particles in the cathode composite and generate the XPEEM images in Figure 3. True intensities were used in the color maps for the $Ni^{2+/3+}$ (magenta) and conductive carbon (cyan) (Figure 3). For XPEEM maps of the Ni L-edge, the Ni⁴⁺ maps' (850.0 eV, dark blue) image intensities were renormalized to emphasize the changing ratio between the two L₃ edge peaks upon charge. The real intensity values of the Ni⁴⁺ maps were multiplied by the ratio obtained from dividing the maximum intensity of the Ni L-edge component at 855.8 eV (Ni^{3+/4+}) by the component at 853.4 eV (Ni²⁺) in Figure S12. The LiF map in Figure 3b was produced by subtracting the LiF slice at 702.0 eV from the slice at 689.0 eV (corresponding to the left shoulder of the PVDF peak) to remove the contribution from PVDF to the LiF slice while avoiding subtraction of the low-intensity LiF peak that may overlap with PVDF sites. (Figure 3c shows that the broad PVDF peak has a shoulder that slightly overlaps with the LiF peak). The resulting LiF image was then thresholded

to only show high-intensity regions, ultimately producing a single intensity map that indicates the spatial distribution of high LiF regions.

Analysis of the Ni L-edge XAS spectra supports the presence of a thin Ni²⁺ reconstruction layer on the cycled sample based on the fact that the peak intensity of the Ni^{2+/3+} transition (853.5 eV) is higher than that of the Ni⁴⁺ transition (855.9 eV)³¹ even on the delithiated sample (Figure 3a, bottom, and Figure S12, note that XPEEM is a surface-sensitive technique and does not represent bulk oxidation states). In the pristine NMC811 film (Figure 3a, top), we observe a heterogeneous distribution of carbon about the NMC particles. Dark regions at the top right of the pristine film correspond to the location of Au particles used for C K-edge normalization (see the Materials and Methods section). After 50 cycles (Figure 3a, bottom), additional dark regions are observed due to the surface roughening that occurs during electrochemical cycling.

Figure 3b shows the F K-edge elemental maps that depict the spatial distribution of LiF with respect to NMC811 and the carbon additives after 50 galvanostatic cycles and disassembled at 4.6 V; representative local XAS spectra are shown in Figure 3c. Both F K-edge spectra from NMC particles and carbon additives show a broad peak at 693 eV that corresponds to the PVDF binder distributed throughout the composite, which is supported by the location of PVDF seen in XPEEM maps from F K-edge spectra (Figures S13 and S14) and agrees with prior XPEEM reports on Ni-rich composite cathodes. 58,83 The breadth of the PVDF absorption peak makes it difficult to discern the presence of metal fluoride (MeF_x)-type compounds at 690 eV^{58,83} that are proposed to deposit in the CEI,⁷⁵ although a slight shoulder in this region is more apparent local to the NMC particles (Figure 3c). In contrast, LiF in the CEI shows a distinct peak at 702 eV⁸³ and deposits preferentially on NMC811 particles rather than the carbon additives (Figure

In principle, LiF can be generated from the reaction of surface Li_2CO_3 on NMC811 and HF in the electrolyte as follows

$$\text{Li}_2\text{CO}_3 + 2\text{HF} \rightarrow 2\text{LiF} + \text{H}_2\text{O} + \text{CO}_2$$

In situ ¹⁹F solution NMR detects HF at $-190 \text{ ppm}^{19,84,85}$ upon electrochemical cycling of Li/NMC811 half-cells (Figure 4). The resonance at -85.2 ppm (d, $J_{P-F} = 930 \text{ Hz}$) is assigned to PF₂O₂⁻, a reaction product from hydrolysis of PF₆⁻. Small

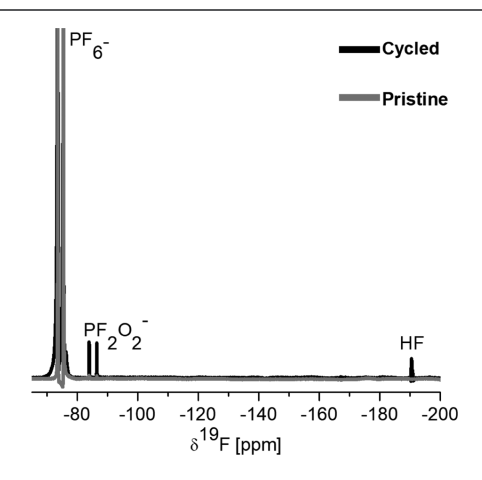


Figure 4. *In situ* solution ¹⁹F NMR from an NMC811/Li battery in an NMR tube cell after 10 galvanostatic cycles at C/10 from 3.0 to 4.6 V.

quantities of $PF_2O_2^-$ are also observed in the pristine electrolyte, indicating that this compound is produced from trace water in the as-purchased, battery-grade electrolyte. ^{18,19,86} On the other hand, the presence of HF could only be observed with *in situ* metrology, which is consistent with the reactive nature of HF. No HF is detected in the pristine electrolyte, indicating that HF is primarily generated from hydrolysis of LiPF₆ upon electrolyte oxidation rather than from trace water in the battery-grade electrolyte. Oxidation of EC and DMC solvents is proposed to produce carboxylic acids, CO_2 , and $H_2O._2^{9,19}$ This H_2O then serves as the source of LiPF₆ hydrolysis that forms HF. Once HF is present in the electrolyte, it reacts with Li₂CO₃ on the surface of NMC811 to form LiF that remains directly attached to the active material during battery operation.

Local C K-edge XAS (Figure S15) spectra from the XPEEM images on the cycled NMC sample indicate that organic carbonate structures are deposited on both NMC as well as the carbon additives. The C K-edge spectra are dominated by peaks from conductive carbon at 285.4 and 291.9 eV that correspond to π^* and σ^* transitions, respectively.³⁷ Regions corresponding to π^* and σ^* transitions are also observed on the NMC particles, suggesting that conductive carbon is also present in these regions and/or these XAS features arise from other sp² hybridized carbon molecules in the CEI layer (e.g., vinyl species). Local C K-edge spectra extracted from pristine NMC811 particles also exhibit a shoulder at 290.4 eV that is assigned to Li₂CO₃. 58,59 This assignment is consistent with the spinning sideband pattern observed for Li₂CO₃ in ¹³C SSNMR as well as the location of LiF on NMC811 (that we believe is generated from Li₂CO₃). Upon electrochemical cycling, we observe a more clearly defined peak at 290.8 eV on both NMC and the conductive carbon that may correspond to the EC/ DMC-derived species observed in SSNMR (e.g., alkyl carbonates, DMDOHD). 59,87 Likewise, the broad absorption at 287.5 eV is assigned aliphatic carbon environments from these short-chain alkyl carbonates as well as the PVDF binder. 59,88,89 Taken together, the C K-edge results indicate that alkyl carbonates deposit on both the carbon and the active material, and are consistent with the soluble nature of these species in the outer CEI, 40,41 such as DMDOHD, which is also detected in solution NMR experiments (Figure S7). We suspect that these organic molecules are distributed randomly across the cathode film as a result of their solubility, indicating that they desorb from the interphase and fail to protect the cathode during electrochemical cycling. 40,41

DISCUSSION

Figure 5 summarizes the chemical insight gained from SSNMR, in situ solution NMR, and XPEEM on the radial and lateral arrangement of the CEI on NMC811 composite films. Coupling to residual paramagnetic centers in NMC811 (e.g., Mn⁴⁺ and surface NiO) after electrochemical cycling leads to spinning sideband patterns for Li₂CO₃ and carboxycontaining compounds in the CEI that are attached to the surface of active particles. Based on both XPEEM and SSNMR, we believe that Li₂CO₃ is present as a native CEI component on pristine NMC811 (leftover from synthesis or from exposure to moisture⁹⁰) that can be altered during electrolyte oxidation. Electrolyte solvent oxidation at the cathode produces particle-bound carboxy-containing CEI compounds, water, and CO₂. The water produced during these reactions hydrolyzes LiPF₆ salt in the electrolyte, forming HF that can attack Li₂CO₃ and

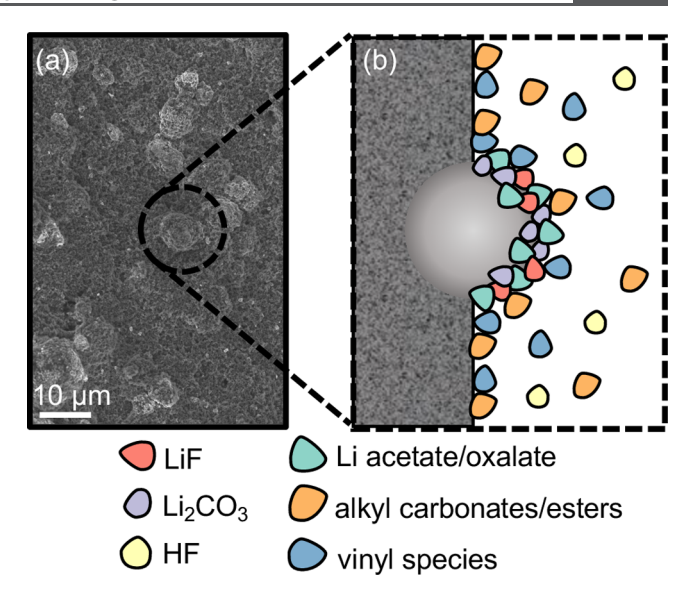


Figure 5. (a) Scanning electron microscopy (SEM) image of the surface of an NMC811 composite cathode film, with an NMC particle circled. (b) Schematic diagram depicting how the CEI is deposited on a composite cathode film during electrochemical cycling. It shows the cross section of the electrolyte-facing cathode film. An NMC811 particle is shown as a light gray sphere, carbon additives are shown in speckled gray, and the electrolyte is shown in white.

lead to the NMC811-bound LiF detected in XPEEM. Note that some Li₂CO₃ is likely still bound to the NMC811 surface after electrochemical cycling, as indicated by ¹³C SSNMR measurements, but cannot be resolved due to spectral overlap with other CEI components in C K-edge spectra. The presence of high quantities of organic carbonates in the CEI on Ni-rich cathodes is consistent with findings from Manthiram and coworkers who used a combination of X-ray photoelectron spectroscopy (XPS) and time-of-flight secondary ion mass spectrometry (TOF-SIMS) to show that oxygen evolution at high voltages produces numerous carbonate-containing structures.⁹¹ Electrolyte oxidation at the cathode also produces highly soluble CEI components such as unsaturated carbons (e.g., VC and linear vinyl compounds observed here with in situ NMR that possibly arise from solvent dehydrogenation⁴) and short-chain alkyl carbonates (e.g., DMDOHD) that fail to passivate the active material. Prior work from Shao-Horn and co-workers suggests that the formation of these vinyl species is correlated with higher Ni content active materials and leads to performance decline during usage. 4,33 Strategies that mitigate interaction between the Ni-rich surface and the liquid electrolyte (e.g., coatings) are expected to prevent the formation of these soluble decomposition products and improve LIB performance.

These findings on electrolyte oxidation and the ultimate impact on CEI compositional arrangement were uniquely enabled by the complementary nature of *ex/in situ* NMR and XPEEM. Unlike X-ray methods that require ultrahigh vacuum conditions, NMR is less destructive and for *in situ* measurements, completely noninvasive. NMR also eliminates the need for rinsing during sample preparation, making it ideal for identifying sensitive organic species in the CEI that are soluble or that may be destroyed via X-ray irradiation. Conversely, since samples are washed prior to XPEEM analyses to prevent outgassing, this technique is well suited to studying insoluble CEI species (e.g., LiF) especially when detection with NMR is

challenging due to strong dipolar interactions between the substrate and high gyromagnetic ratio nuclei in the material of interest (e.g., Li¹⁹F). Overall, the combination of NMR and XPEEM allows a comprehensive description of the radial and lateral arrangement of the heterogeneous CEI layer on NMC811 that can be extended to other composite cathode compositions to describe structure—property—performance relationships in these systems.

CONCLUSIONS

We demonstrate that SSNMR can be used to analyze the radial arrangement of the CEI from active material particles in Nirich composite cathode films. EPR measurements indicate that high-resolution SSNMR is enabled by dilution of the paramagnetic matrix upon oxidation of $\mathrm{Ni}^{2+/3+}$ to Ni^{4+} and can likely be extended to other Ni-rich transition-metal oxides that are of technological interest (e.g., $\text{LiNi}_{1-x-y}\text{Co}_x\text{Al}_y\text{O}_2$). XPEEM imaging complements SSNMR measurements by confirming the lateral distribution of electrolyte decomposition products on the composite surface, where the reaction of residual Li₂CO₃ generates an active material-bound CEI layer consisting of insoluble LiF. Soluble organic compounds in the CEI can detach from the particle surface and randomly deposit on the outer CEI of the active material as well as the carbon additives. The detection of many soluble electrolyte oxidation products (e.g., vinyl groups and HF) was accomplished via in situ NMR spectroscopy and provided key evidence of reactions between the active material, CO2, and water that lead to the resulting CEI compositional arrangement. The molecular-level information provided by SSNMR and XPEEM can be leveraged to provide mechanistic insight into how specific cycling protocols (e.g., altering upper cutoff voltage) and coating strategies may alleviate particular modes of battery degradation. More broadly, we expect that these techniques can be extended to monitor chemical reactivity at complex electrochemical interfaces used in a wide range of applications for energy storage, conversion, and harvesting.

ASSOCIATED CONTENT

Supporting Information

The Supporting Information is available free of charge at https://pubs.acs.org/doi/10.1021/acs.chemmater.1c03185.

Electrochemical cycling data, EPR spectra, solution NMR spectra, SSNMR spectra, 1 H T_{1} relaxometry results, XPEEM results, and associated XAS spectra (PDF)

AUTHOR INFORMATION

Corresponding Author

Lauren E. Marbella — Department of Chemical Engineering, Columbia University, New York, New York 10027, United States; orcid.org/0000-0003-1639-3913; Email: lem2221@columbia.edu

Authors

Julia C. Hestenes — Program of Materials Science and Engineering, Department of Applied Physics and Applied Mathematics, Columbia University, New York, New York 10027, United States

Richard May — Department of Chemical Engineering, Columbia University, New York, New York 10027, United States Jerzy T. Sadowski — Center for Functional Nanomaterials, Brookhaven National Laboratory, Upton, New York 11973, United States; Occid.org/0000-0002-4365-7796

Naiara Munich — Department of Chemistry, Barnard College of Columbia University, New York, New York 10027, United States

Complete contact information is available at: https://pubs.acs.org/10.1021/acs.chemmater.1c03185

Notes

The authors declare no competing financial interest.

ACKNOWLEDGMENTS

This work was supported by National Science Foundation CAREER Award (CBET-2045262). This research used resources of the Center for Functional Nanomaterials and the National Synchrotron Light Source II, which are U.S. Department of Energy (DOE) Office of Science facilities at Brookhaven National Laboratory, under Contract No. DE-SC0012704. L.E.M. acknowledges support from Columbia University's Provost Grants Program for Junior Faculty who Contribute to the Diversity Goals of the University. J.C.H. was supported by the National Science Foundation Graduate Research Fellowship Program (NSF GRFP # 2021278071). R.M. was supported by the U.S. Department of Defense through the National Defense Science & Engineering Graduate (NDSEG) Fellowship Program. N.M. was supported by the Science Pathways Scholars Program of Barnard College of Columbia University.

REFERENCES

- (1) Kasnatscheew, J.; Röser, S.; Börner, M.; Winter, M. Do Increased Ni Contents in $\text{LiNi}_X \text{Mn}_Y \text{Co}_Z \text{O}_2$ (NMC) Electrodes Decrease Structural and Thermal Stability of Li Ion Batteries? A Thorough Look by Consideration of the Li⁺ Extraction Ratio. *ACS Appl. Energy Mater.* **2019**, *2*, 7733–7737.
- (2) Li, T.; Yuan, X.-Z.; Zhang, L.; Song, D.; Shi, K.; Bock, C. Degradation Mechanisms and Mitigation Strategies of Nickel-Rich NMC-Based Lithium-Ion Batteries. *Electrochem. Energy Rev.* **2020**, 3, 43–80
- (3) Gourley, S. W. D.; Or, T.; Chen, Z. Breaking Free from Cobalt Reliance in Lithium-Ion Batteries. *iScience* **2020**, 23, No. 101505.
- (4) Zhang, Y.; Katayama, Y.; Tatara, R.; Giordano, L.; Yu, Y.; Fraggedakis, D.; Sun, J. G.; Maglia, F.; Jung, R.; Bazant, M. Z.; Shao-Horn, Y. Revealing Electrolyte Oxidation: Via Carbonate Dehydrogenation on Ni-Based Oxides in Li-Ion Batteries by in Situ Fourier Transform Infrared Spectroscopy. *Energy Environ. Sci.* 2020, 13, 183–100.
- (5) Sun, H. H.; Manthiram, A. Impact of Microcrack Generation and Surface Degradation on a Nickel-Rich Layered Li[Ni_{0.9}Co_{0.05}Mn_{0.05}]-O₂ Cathode for Lithium-Ion Batteries. *Chem. Mater.* **2017**, 29, 8486–8493.
- (6) Ryu, H. H.; Park, K. J.; Yoon, C. S.; Sun, Y. K. Capacity Fading of Ni-Rich $\text{Li}[\text{Ni}_x\text{Co}_y\text{Mn}_{1-x-y}]\text{O}_2$ (0.6 \leq x \leq 0.95) Cathodes for High-Energy-Density Lithium-Ion Batteries: Bulk or Surface Degradation? *Chem. Mater.* **2018**, 30, 1155–1163.
- (7) Yan, P.; Zheng, J.; Gu, M.; Xiao, J.; Zhang, J.-G.; Wang, C.-M. Intragranular Cracking as a Critical Barrier for High-Voltage Usage of Layer-Structured Cathode for Lithium-Ion Batteries. *Nat. Commun.* **2017**, *8*, No. 14101.
- (8) Xu, Z.; Rahman, M. M.; Mu, L.; Liu, Y.; Lin, F. Chemomechanical Behaviors of Layered Cathode Materials in Alkali Metal Ion Batteries. *J. Mater. Chem. A* **2018**, *6*, 21859–21884.
- (9) Jung, R.; Metzger, M.; Maglia, F.; Stinner, C.; Gasteiger, H. A. Oxygen Release and Its Effect on the Cycling Stability of

- LiNi_xMn_yCo_zO₂ (NMC) Cathode Materials for Li-Ion Batteries. *J. Electrochem. Soc.* **2017**, *164*, A1361–A1377.
- (10) Renfrew, S. E.; McCloskey, B. D. Residual Lithium Carbonate Predominantly Accounts for First Cycle CO₂ and CO Outgassing of Li-Stoichiometric and Li-Rich Layered Transition-Metal Oxides. *J. Am. Chem. Soc.* **2017**, *139*, 17853–17860.
- (11) Kong, F.; Liang, C.; Wang, L.; Zheng, Y.; Perananthan, S.; Longo, R. C.; Ferraris, J. P.; Kim, M.; Cho, K. Kinetic Stability of Bulk LiNiO₂ and Surface Degradation by Oxygen Evolution in LiNiO₂-Based Cathode Materials. *Adv. Energy Mater.* **2019**, *9*, No. 1802586.
- (12) Lin, F.; Markus, I. M.; Nordlund, D.; Weng, T. C.; Asta, M. D.; Xin, H. L.; Doeff, M. M. Surface Reconstruction and Chemical Evolution of Stoichiometric Layered Cathode Materials for Lithium-Ion Batteries. *Nat. Commun.* **2014**, *5*, No. 3529.
- (13) Xu, C.; Märker, K.; Lee, J.; Mahadevegowda, A.; Reeves, P. J.; Day, S. J.; Groh, M. F.; Emge, S. P.; Ducati, C.; Layla Mehdi, B.; Tang, C. C.; Grey, C. P. Bulk Fatigue Induced by Surface Reconstruction in Layered Ni-Rich Cathodes for Li-Ion Batteries. *Nat. Mater.* 2020, 20, 84–92.
- (14) Carroll, K. J.; Qian, D.; Fell, C.; Calvin, S.; Veith, G. M.; Chi, M.; Baggetto, L.; Meng, Y. S. Probing the Electrode/Electrolyte Interface in the Lithium Excess Layered Oxide Li_{1.2}Ni_{0.2}Mn_{0.6}O₂. *Phys. Chem. Chem. Phys.* **2013**, *15*, 11128–11138.
- (15) Wandt, J.; Freiberg, A.; Thomas, R.; Gorlin, Y.; Siebel, A.; Jung, R.; Gasteiger, H. A.; Tromp, M. Transition Metal Dissolution and Deposition in Li-Ion Batteries Investigated by Operando X-Ray Absorption Spectroscopy. *J. Mater. Chem. A* **2016**, *4*, 18300–18305.
- (16) Li, W.; Dolocan, A.; Oh, P.; Celio, H.; Park, S.; Cho, J.; Manthiram, A. Dynamic Behaviour of Interphases and Its Implication on High-Energy-Density Cathode Materials in Lithium-Ion Batteries. *Nat. Commun.* **2017**, *8*, No. 14589.
- (17) Su, C.-C.; He, M.; Amine, R.; Chen, Z.; Yu, Z.; Rojas, T.; Cheng, L.; Ngo, A. T.; Amine, K. Unveiling Decaying Mechanism through Quantitative Structure-Activity Relationship in Electrolytes for Lithium-Ion Batteries. *Nano Energy* **2021**, *83*, No. 105843.
- (18) Yu, Y.; Karayaylali, P.; Katayama, Y.; Giordano, L.; Gauthier, M.; Maglia, F.; Jung, R.; Lund, I.; Shao-Horn, Y. Coupled LiPF₆ Decomposition and Carbonate Dehydrogenation Enhanced by Highly Covalent Metal Oxides in High-Energy Li-Ion Batteries. *J. Phys. Chem.* C 2018, 122, 27368–27382.
- (19) Rinkel, B.; Hall, D. S.; Temprano, I.; Grey, C. P. Electrolyte Oxidation Pathways in Lithium-Ion Batteries. *J. Am. Chem. Soc.* **2020**, *142*, 15058–15074.
- (20) Ohzuku, T.; Ueda, A.; Nagayama, M. Electrochemistry and Structural Chemistry of LiNiO₂ (*R*3*m*) for 4 Volt Secondary Lithium Cells. *J. Electrochem. Soc.* **1993**, 140, 1862.
- (21) Yoon, C. S.; Jun, D.-W.; Myung, S.-T.; Sun, Y.-K. Structural Stability of LiNiO₂ Cycled above 4.2 V. ACS Energy Lett. **2017**, 2, 1150–1155.
- (22) Märker, K.; Reeves, P. J.; Xu, C.; Griffith, K. J.; Grey, C. P. Evolution of Structure and Lithium Dynamics in LiNi_{0.8}Mn_{0.1}Co_{0.1}O₂ (NMC811) Cathodes during Electrochemical Cycling. *Chem. Mater.* **2019**. *31*. 2545–2554.
- (23) Hy, S.; Liu, H.; Zhang, M.; Qian, D.; Hwang, B. J.; Meng, Y. S. Performance and Design Considerations for Lithium Excess Layered Oxide Positive Electrode Materials for Lithium Ion Batteries. *Energy Environ. Sci.* **2016**, *9*, 1931–1954.
- (24) Noh, H. J.; Youn, S.; Yoon, C. S.; Sun, Y. K. Comparison of the Structural and Electrochemical Properties of Layered Li[Ni_xCo_yMn_z]-O₂ (x = 1/3, 0.5, 0.6, 0.7, 0.8 and 0.85) Cathode Material for Lithium-Ion Batteries. *J. Power Sources* **2013**, 233, 121–130.
- (25) Xia, S.; Mu, L.; Xu, Z.; Wang, J.; Wei, C.; Liu, L.; Pianetta, P.; Zhao, K.; Yu, X.; Lin, F.; Liu, Y. Chemomechanical Interplay of Layered Cathode Materials Undergoing Fast Charging in Lithium Batteries. *Nano Energy* **2018**, *53*, 753–762.
- (26) Gauthier, M.; Carney, T. J.; Grimaud, A.; Giordano, L.; Pour, N.; Chang, H. H.; Fenning, D. P.; Lux, S. F.; Paschos, O.; Bauer, C.; Maglia, F.; Lupart, S.; Lamp, P.; Shao-Horn, Y. Electrode-Electrolyte

- Interface in Li-Ion Batteries: Current Understanding and New Insights. J. Phys. Chem. Lett. 2015, 6, 4653–4672.
- (27) Strehle, B.; Kleiner, K.; Jung, R.; Chesneau, F.; Mendez, M.; Gasteiger, H. A.; Piana, M. The Role of Oxygen Release from Li- and Mn-Rich Layered Oxides during the First Cycles Investigated by On-Line Electrochemical Mass Spectrometry. *J. Electrochem. Soc.* **2017**, *164*, A400–A406.
- (28) Streich, D.; Erk, C.; Guéguen, A.; Müller, P.; Chesneau, F. F.; Berg, E. J. Operando Monitoring of Early Ni-Mediated Surface Reconstruction in Layered Lithiated Ni-Co-Mn Oxides. *J. Phys. Chem.* C 2017, 121, 13481–13486.
- (29) Berkes, B. B.; Schiele, A.; Sommer, H.; Brezesinski, T.; Janek, J. On the Gassing Behavior of Lithium-Ion Batteries with NCM523 Cathodes. *J. Solid State Electrochem.* **2016**, 20, 2961–2967.
- (30) Schipper, F.; Erickson, E. M.; Erk, C.; Shin, J.-Y.; Chesneau, F. F.; Aurbach, D. Review—Recent Advances and Remaining Challenges for Lithium Ion Battery Cathodes. *J. Electrochem. Soc.* **2017**, *164*, A6220—A6228.
- (31) Yu, Y.; Karayaylali, P.; Giordano, L.; Corchado-Garciá, J.; Hwang, J.; Sokaras, D.; Maglia, F.; Jung, R.; Gittleson, F. S.; Shao-Horn, Y. Probing Depth-Dependent Transition-Metal Redox of Lithium Nickel, Manganese, and Cobalt Oxides in Li-Ion Batteries. ACS Appl. Mater. Interfaces 2020, 12, 55865–55875.
- (32) Manthiram, A. An Outlook on Lithium Ion Battery Technology. ACS Cent. Sci. 2017, 3, 1063-1069.
- (33) Giordano, L.; Karayaylali, P.; Yu, Y.; Katayama, Y.; Maglia, F.; Lux, S.; Shao-Horn, Y. Chemical Reactivity Descriptor for the Oxide-Electrolyte Interface in Li-Ion Batteries. *J. Phys. Chem. Lett.* **2017**, *8*, 3881–3887.
- (34) Edström, K.; Gustafsson, T.; Thomas, J. O. The Cathode-Electrolyte Interface in the Li-Ion Battery. *Electrochim. Acta* **2004**, *50*, 397–403.
- (35) Demeaux, J.; Caillon-Caravanier, M.; Galiano, H.; Lemordant, D.; Claude-Montigny, B. LiNi_{0.4}Mn_{1.6}O₄ /Electrolyte and Carbon Black/Electrolyte High Voltage Interfaces: To Evidence the Chemical and Electronic Contributions of the Solvent on the Cathode-Electrolyte Interface Formation. *J. Electrochem. Soc.* **2012**, *159*, A1880–A1890.
- (36) Metzger, M.; Marino, C.; Sicklinger, J.; Haering, D.; Gasteiger, H. A. Anodic Oxidation of Conductive Carbon and Ethylene Carbonate in High-Voltage Li-Ion Batteries Quantified by On-Line Electrochemical Mass Spectrometry. *J. Electrochem. Soc.* **2015**, *162*, A1123—A1134.
- (37) Mirolo, M.; Leanza, D.; Höltschi, L.; Jordy, C.; Pelé, V.; Novák, P.; El Kazzi, M.; Vaz, C. A. F. Post Mortem and Operando XPEEM: A Surface-Sensitive Tool for Studying Single Particles in Li-Ion Battery Composite Electrodes. *Anal. Chem.* **2020**, *92*, 3023–3031.
- (38) Li, J.; Manthiram, A. A Comprehensive Analysis of the Interphasial and Structural Evolution over Long-Term Cycling of Ultrahigh-Nickel Cathodes in Lithium-Ion Batteries. *Adv. Energy Mater.* **2019**, *9*, No. 1902731.
- (39) Leanza, D.; Vaz, C. A. F.; Novák, P.; El Kazzi, M. Instability of PVDF Binder in the LiFePO₄ versus Li₄Ti₅O₁₂ Li-Ion Battery Cell. *Helv. Chim. Acta* **2021**, *104*, No. e2000183.
- (40) Fang, S.; Jackson, D.; Dreibelbis, M. L.; Kuech, T. F.; Hamers, R. J. Anode-Originated SEI Migration Contributes to Formation of Cathode-Electrolyte Interphase Layer. *J. Power Sources* **2018**, 373, 184–192.
- (41) Hestenes, J. C.; Ells, A. W.; Navarro Goldaraz, M.; Sergeyev, I. V.; Itin, B.; Marbella, L. E. Reversible Deposition and Stripping of the Cathode Electrolyte Interphase on Li₂RuO₃. *Front. Chem.* **2020**, 8, No. 681.
- (42) Betz, J.; Brinkmann, J. P.; Nölle, R.; Lürenbaum, C.; Kolek, M.; Stan, M. C.; Winter, M.; Placke, T. Cross Talk between Transition Metal Cathode and Li Metal Anode: Unraveling Its Influence on the Deposition/Dissolution Behavior and Morphology of Lithium. *Adv. Energy Mater.* **2019**, *9*, No. 1900574.

- (43) Langdon, J.; Manthiram, A. Crossover Effects in Batteries with High-Nickel Cathodes and Lithium-Metal Anodes. *Adv. Funct. Mater.* **2021**, *31*, No. 2010267.
- (44) Michan, A. L.; Leskes, M.; Grey, C. P. Voltage Dependent Solid Electrolyte Interphase Formation in Silicon Electrodes: Monitoring the Formation of Organic Decomposition Products. *Chem. Mater.* **2016**, 28, 385–398.
- (45) Jin, Y.; Kneusels, N. J. H.; Magusin, P. C. M. M.; Kim, G.; Castillo-Martínez, E.; Marbella, L. E.; Kerber, R. N.; Howe, D. J.; Paul, S.; Liu, T.; Grey, C. P. Identifying the Structural Basis for the Increased Stability of the Solid Electrolyte Interphase Formed on Silicon with the Additive Fluoroethylene Carbonate. *J. Am. Chem. Soc.* 2017, 139, 14992–15004.
- (46) Jin, Y.; Kneusels, N. J. H.; Marbella, L. E.; Castillo-Martínez, E.; Magusin, P. C. M. M.; Weatherup, R. S.; Jónsson, E.; Liu, T.; Paul, S.; Grey, C. P. Understanding Fluoroethylene Carbonate and Vinylene Carbonate Based Electrolytes for Si Anodes in Lithium Ion Batteries with NMR Spectroscopy. J. Am. Chem. Soc. 2018, 140, 9854–9867.
- (47) May, R.; Zhang, Y.; Denny, S. R.; Viswanathan, V.; Marbella, L. E. Leveraging Cation Identity to Engineer Solid Electrolyte Interphases for Rechargeable Lithium Metal Anodes. *Cell Rep. Phys. Sci.* **2020**, *1*, No. 100239.
- (48) Leskes, M.; Kim, G.; Liu, T.; Michan, A. L.; Aussenac, F.; Dorffer, P.; Paul, S.; Grey, C. P. Surface-Sensitive NMR Detection of the Solid Electrolyte Interphase Layer on Reduced Graphene Oxide. *J. Phys. Chem. Lett.* **2017**, *8*, 1078–1085.
- (49) Michan, A. L.; Divitini, G.; Pell, A. J.; Leskes, M.; Ducati, C.; Grey, C. P. Solid Electrolyte Interphase Growth and Capacity Loss in Silicon Electrodes. *J. Am. Chem. Soc.* **2016**, *138*, 7918–7931.
- (50) Cuisinier, M.; Dupré, N.; Martin, J. F.; Kanno, R.; Guyomard, D. Evolution of the LiFePO₄ Positive Electrode Interface along Cycling Monitored by MAS NMR. *J. Power Sources* **2013**, 224, 50–58.
- (51) Dupré, N.; Martin, J.-F.; Oliveri, J.; Soudan, P.; Guyomard, D.; Yamada, A.; Kanno, R. Aging of the LiNi_{1/2}Mn_{1/2}O₂ Positive Electrode Interface in Electrolyte. *J. Electrochem. Soc.* **2009**, 156,
- (52) Haber, S.; Leskes, M. What Can We Learn from Solid State NMR on the Electrode–Electrolyte Interface? *Adv. Mater.* **2018**, *30*, No. 1706496.
- (53) Dupre, N.; Cuisinier, M.; Guyomard, D. Electrode/Electrolyte Interface Studies in Lithium Batteries Using NMR. *Electrochem. Soc. Interface* **2011**, *20*, 61–67.
- (54) Grey, C. P.; Dupré, N. NMR Studies of Cathode Materials for Lithium-Ion Rechargeable Batteries. *Chem. Rev.* **2004**, *104*, 4493–4512.
- (55) Dupré, N.; Martin, J. F.; Guyomard, D.; Yamada, A.; Kanno, R. Detection of Surface Layers Using ^7Li MAS NMR. *J. Mater. Chem.* **2008**, *18*, 4266–4273.
- (56) Cuisinier, M.; Martin, J. F.; Moreau, P.; Epicier, T.; Kanno, R.; Guyomard, D.; Dupré, N. Quantitative MAS NMR Characterization of the $LiMn_{1/2}Ni_{1/2}O_2$ Electrode/Electrolyte Interphase. *Solid State Nucl. Magn. Reson.* **2012**, 42, 51–61.
- (57) Pell, A. J.; Pintacuda, G.; Grey, C. P. Paramagnetic NMR in Solution and the Solid State. *Prog. Nucl. Magn. Reson. Spectrosc.* **2019**, 111, 1–271.
- (58) Mirolo, M.; Vaz, C. A. F.; Novák, P.; El Kazzi, M. Multi-Length-Scale x-Ray Spectroscopies for Determination of Surface Reactivity at High Voltages of LiNi_{0.8}Co_{0.15}Al_{0.05}O₂ vs Li₄Ti₅O₁₂. *J. Chem. Phys.* **2020**, *152*, No. 184705.
- (59) Zhuo, Z.; Lu, P.; Delacourt, C.; Qiao, R.; Xu, K.; Pan, F.; Harris, S. J.; Yang, W. Breathing and Oscillating Growth of Solid-Electrolyte-Interphase upon Electrochemical Cycling. *Chem. Commun.* **2018**, *54*, 814–817.
- (60) Wiemers-Meyer, S.; Winter, M.; Nowak, S. A Battery Cell for in Situ NMR Measurements of Liquid Electrolytes. *Phys. Chem. Chem. Phys.* **2017**, *19*, 4962–4966.
- (61) Zhou, L.; Leskes, M.; Liu, T.; Grey, C. P. Probing Dynamic Processes in Lithium-Ion Batteries by in Situ NMR Spectroscopy:

- Application to $Li_{1.08}Mn_{1.92}O_4$ Electrodes. Angew. Chem., Int. Ed. **2015**, 54, 14782–14786.
- (62) Nguyen, H.; Clément, R. J. Rechargeable Batteries from the Perspective of the Electron Spin. ACS Energy Lett. 2020, 5, 3848–3859
- (63) Shinova, E.; Stoyanova, R.; Zhecheva, E.; Ortiz, G. F.; Lavela, P.; Tirado, J. L. Cationic Distribution and Electrochemical Performance of $\text{LiCo}_{1/3}\text{Ni}_{1/3}\text{Mn}_{1/3}\text{O}_2$ Electrodes for Lithium-Ion Batteries. *Solid State Ionics* **2008**, *179*, 2198–2208.
- (64) Tang, M.; Dalzini, A.; Li, X.; Feng, X.; Chien, P. H.; Song, L.; Hu, Y. Y. Operando EPR for Simultaneous Monitoring of Anionic and Cationic Redox Processes in Li-Rich Metal Oxide Cathodes. *J. Phys. Chem. Lett.* **2017**, *8*, 4009–4016.
- (65) Mukherjee, P.; Paddison, J. A. M.; Xu, C.; Ruff, Z.; Wildes, A. R.; Keen, D. A.; Smith, R. I.; Grey, C. P.; Dutton, S. E. Sample Dependence of Magnetism in the Next-Generation Cathode Material LiNi_{0.8}Mn_{0.1}Co_{0.1}O₂. *Inorg. Chem.* **2021**, *60*, 263–271.
- (66) Flores, E.; Novák, P.; Aschauer, U.; Berg, E. J. Cation Ordering and Redox Chemistry of Layered Ni-Rich Li_XNi_{1-2Y}Co_YMn_YO₂: An Operando Raman Spectroscopy Study. *Chem. Mater.* **2020**, 32, 186–194
- (67) Sclar, H.; Kovacheva, D.; Zhecheva, E.; Stoyanova, R.; Lavi, R.; Kimmel, G.; Grinblat, J.; Girshevitz, O.; Amalraj, F.; Haik, O.; Zinigrad, E.; Markovsky, B.; Aurbach, D. On the Performance of $\text{LiNi}_{1/3}\text{Mn}_{1/3}\text{Co}_{1/3}\text{O}_2$ Nanoparticles as a Cathode Material for Lithium-Ion Batteries. *J. Electrochem. Soc.* **2009**, *156*, A938.
- (68) Stoyanova, R.; Barra, A. L.; Yoncheva, M.; Zhecheva, E.; Shinova, E.; Tzvetkova, P.; Simova, S. High-Frequency Electron Paramagnetic Resonance Analysis of the Oxidation State and Local Structure of Ni and Mn Ions in Ni, Mn-Codoped LiCoO₂. *Inorg. Chem.* **2010**, *49*, 1932–1941.
- (69) Chernova, N. A.; Ma, M.; Xiao, J.; Whittingham, M. S.; Breger, J.; Grey, C. P. Layered Li_xNi_yMn_yCo_{1-2y}O₂ Cathodes for Lithium Ion Batteries: Understanding Local Structure via Magnetic Properties. *Chem. Mater.* **2007**, *19*, 4682–4693.
- (70) Niemöller, A.; Jakes, P.; Eurich, S.; Paulus, A.; Kungl, H.; Eichel, R. A.; Granwehr, J. Monitoring Local Redox Processes in LiNi_{0.5}Mn_{1.5}O₄ Battery Cathode Material by in Operando EPR Spectroscopy. *J. Chem. Phys.* **2018**, *148*, No. 014705.
- (71) El Mofid, W.; Ivanov, S.; Konkin, A.; Bund, A. A High Performance Layered Transition Metal Oxide Cathode Material Obtained by Simultaneous Aluminum and Iron Cationic Substitution. *J. Power Sources* **2014**, *268*, 414–422.
- (72) Hwang, B. J.; Tsai, Y. W.; Carlier, D.; Ceder, G. A Combined Computational/Experimental Study on LiNi_{1/3}Co_{1/3}Mn_{1/3}O₂. *Chem. Mater.* **2003**, *15*, 3676–3682.
- (73) Mauger, A.; Gendron, F.; Julien, C. M. Magnetic Properties of $Li_XNi_YMn_YCo_{1-2y}O_2$ (0.2 \leq 1 2y \leq 0.5, 0 \leq x \leq 1). *J. Alloys Compd.* **2012**, 520, 42–51.
- (74) Liu, H.; Bugnet, M.; Tessaro, M. Z.; Harris, K. J.; Dunham, M. J. R.; Jiang, M.; Goward, G. R.; Botton, G. A. Spatially Resolved Surface Valence Gradient and Structural Transformation of Lithium Transition Metal Oxides in Lithium-Ion Batteries. *Phys. Chem. Chem. Phys.* **2016**, *18*, 29064–29075.
- (75) Li, W.; Liu, X.; Xie, Q.; You, Y.; Chi, M.; Manthiram, A. Long-Term Cyclability of NCM-811 at High Voltages in Lithium-Ion Batteries: An In-Depth Diagnostic Study. *Chem. Mater.* **2020**, *32*, 7796–7804.
- (76) Tian, C.; Lin, F.; Doeff, M. M. Electrochemical Characteristics of Layered Transition Metal Oxide Cathode Materials for Lithium Ion Batteries: Surface, Bulk Behavior, and Thermal Properties. *Acc. Chem. Res.* 2018, *51*, 89–96.
- (77) Wang, L.; Menakath, A.; Han, F.; Wang, Y.; Zavalij, P. Y.; Gaskell, K. J.; Borodin, O.; Iuga, D.; Brown, S. P.; Wang, C.; Xu, K.; Eichhorn, B. W. Identifying the Components of the Solid–Electrolyte Interphase in Li-Ion Batteries. *Nat. Chem.* **2019**, *11*, 789–796.
- (78) Gachot, G.; Grugeon, S.; Armand, M.; Pilard, S.; Guenot, P.; Tarascon, J. M.; Laruelle, S. Deciphering the Multi-Step Degradation

Mechanisms of Carbonate-Based Electrolyte in Li Batteries. J. Power Sources 2008, 178, 409–421.

- (79) Michan, A. L.; Parimalam, B. S.; Leskes, M.; Kerber, R. N.; Yoon, T.; Grey, C. P.; Lucht, B. L. Fluoroethylene Carbonate and Vinylene Carbonate Reduction: Understanding Lithium-Ion Battery Electrolyte Additives and Solid Electrolyte Interphase Formation. *Chem. Mater.* **2016**, *28*, 8149–8159.
- (80) Simons, W. W. The Sadtler Handbook of Proton NMR Spectra; Sadtler Research Laboratories, 1978.
- (81) Rubinson, K. A.; Rubinson, J. F. Chapter 11, Nuclear Magnetic Resonance Spectrometry. In *Contemporary Instrumental Analysis*; Prentice Hall: Upper Saddle River, New Jersey, 2000; pp 477–513.
- (82) Satterlee, J. D. Fundamental Concepts of NMR in Paramagnetic Systems. Part II: Relaxation Effects. *Concepts Magn. Reson.* **1990**, *2*, 119–129.
- (83) Leanza, D.; Vaz, C. A. F.; Melinte, G.; Mu, X.; Novák, P.; El Kazzi, M. Revealing the Dual Surface Reactions on a HE-NCM Li-Ion Battery Cathode and Their Impact on the Surface Chemistry of the Counter Electrode. ACS Appl. Mater. Interfaces 2019, 11, 6054–6065.
- (84) Parimalam, B. S.; MacIntosh, A. D.; Kadam, R.; Lucht, B. L. Decomposition Reactions of Anode Solid Electrolyte Interphase (SEI) Components with LiPF₆. J. Phys. Chem. C **2017**, 121, 22733–22738.
- (85) Wiemers-Meyer, S.; Winter, M.; Nowak, S. Mechanistic Insights into Lithium Ion Battery Electrolyte Degradation-a Quantitative NMR Study. *Phys. Chem. Chem. Phys.* **2016**, *18*, 26595–26601.
- (86) Plakhotnyk, A. V.; Ernst, L.; Schmutzler, R. Hydrolysis in the System LiPF₆. Propylene Carbonate Dimethyl Carbonate H_2O . *J. Fluorine Chem.* **2005**, *126*, 27–31.
- (87) Li, Q.; Yan, S.; Yang, W. Interfacial Properties in Energy Storage Systems Studied by Soft X-Ray Absorption Spectroscopy and Resonant Inelastic x-Ray Scattering. *J. Chem. Phys.* **2020**, *152*, No. 140901.
- (88) Augustsson, A.; Herstedt, M.; Guo, J. H.; Edström, K.; Zhuang, G. V.; Ross, P. N.; Rubensson, J. E.; Nordgren, J. Solid Electrolyte Interphase on Graphite Li-Ion Battery Anodes Studied by Soft X-Ray Spectroscopy. *Phys. Chem. Chem. Phys.* **2004**, *6*, 4185–4189.
- (89) Williams, R. S.; Denley, D.; Shirley, D. A.; Stöhr, J. Soft X-Ray Absorption Spectroscopy. Electronic and Morphological Structure of Poly(Vinylidene Fluoride). *J. Am. Chem. Soc.* **1980**, *102*, 5717–5723.
- (90) You, Y.; Celio, H.; Li, J.; Dolocan, A.; Manthiram, A. Modified High-Nickel Cathodes with Stable Surface Chemistry Against Ambient Air for Lithium-Ion Batteries. *Angew. Chem., Int. Ed.* **2018**, *57*, 6480–6485.
- (91) Erickson, E. M.; Li, W.; Dolocan, A.; Manthiram, A. Insights into the Cathode-Electrolyte Interphases of High-Energy-Density Cathodes in Lithium-Ion Batteries. *ACS Appl. Mater. Interfaces* **2020**, 12, 16451–16461.